# Resistive Switching in Polyvinylpyrrolidone/Molybdenum Disulfide Composite-Based Memory Devices

Z.W. Dlamini[a,b,*], S. Vallabhapurapu[c], A. Srinivasan[d], S. Wu[e] and V.S. Vallabhapurapu[a]

[a] *Physics Department, College of Science, Engineering, and Technology (CSET), University of South Africa, Pioneer Ave 28, 1710 Johannesburg, South Africa*
[b] *Department of Maths, Science, and Technology Education (MSTE), Faculty of Humanities, Central University of Technology, President Brand 20, 9301 Bloemfontein, South Africa*
[c] *School of Computing, College of Science, Engineering, and Technology (CSET), University of Technology, Pioneer Ave 28, 1710 Johannesburg, South Africa*
[d] *Department of Physics, Indian Institute of Technology Guwahati, Surjyamukhi Road, 781039 Guwahati, India*
[e] *School of Engineering, Faculty of Science and Engineering, Macquarie University, Balaclava Rd, NSW 2109 Sydney, Australia*

Received: 07.08.2021 & Accepted: 03.02.2022

Doi: 10.12693/APhysPolA.141.439 *e-mail: zoliledlamini@hotmail.com

Four types of resistive random access memory structures with an active layer comprising: (1) $MoS_2$ (device A), (2) PVP (device B), (3) PVP and $MoS_2$ bilayer (device C), and (4) PVP + $MoS_2$ nanocomposites with 10 (device D), 20 (device E), 30 (device F) and 40 wt% (device G) $MoS_2$, have been fabricated with Al and Ag as bottom and top electrodes, respectively. A study of resistive switching and electrical conduction mechanisms of these resistive random access memory modules revealed that devices A and B did not exhibit switching characteristics. Device C showed a combination of bipolar and threshold switching with a low switching voltage of 0.40 V. Device G portrayed bipolar switching at 0.56 V. In device C, space charge-limited conduction with a transition voltage $V_{tr} = 0.24$ V was observed, whereas in device G, Ohmic behaviour between 0.0 and 0.22 V, followed by trapping of charge in the 0.22–0.56 V regime before switching, was noticed. Both devices C and G showed a reasonable ($\geq 10^2$) ON/OFF ratio. In nanocomposite devices, an increase in $MoS_2$ content resulted in an increase in electrical conductivity in the Ohmic region, leading to threshold switching at 30 wt% (device F) and ultimately bipolar switching at 40 wt% (device G). These studies have shown that both switching and conduction mechanisms are sensitive to the type and composition of the active layer in the devices studied.

topics: resistive switching, conduction mechanism, $MoS_2$, bilayer

## 1. Introduction

There is a significant increase in data and cloud computing during the fourth industrial revolution [1]. As a result, the current memory technology stands before a serious challenge as ultrafast and high-density memory devices are needed to meet the demand. Furthermore, the current memory technology must reduce its contribution to the growing energy consumption of information and communication technologies (ICT), which currently accounts for more than 3% of global electricity consumption [2]. A complete transformation in memory device technology is needed to meet these demands. Resistive random access memories (ReRAMs) are emerging memories comprising an active layer having two electrically switchable resistive states [3], i.e., a high resistive state (HRS) and a low resistive state (LRS). The active layer is sandwiched between the top electrode (TE) and the bottom electrode (BE) to make a complete memory cell [4, 5]. ReRAMs have advantages such as nonvolatility, low operating voltages, and high endurance, that place them in the spotlight of emerging memory technologies. Additionally, ReRAMs can be made from several materials, so they be compatible with biodegradable [5–11], transparent [8, 9], flexible [10–12], and lightweight electronics [13].

Molybdenum disulfide ($MoS_2$) is a graphene-like 2D transition metal dichalcogenide compound with a layered structure comprising Mo-atom at the centre of a trigonal prism with two sulfur atoms [14]. $MoS_2$ has two variances, i.e., a metallic 1T with octahedral structure and a semiconducting 2H with

TABLE I

Details of the active layers of various devices and resistive switching characteristics.

| Name | Active layer | Switching type |
|---|---|---|
| type I: reference devices | | |
| device A | bare $MoS_2$ | none |
| device B | bare PVP | none |
| type II: bilayer device | | |
| device C | $MoS_2$ and PVP bilayer | bipolar and threshold switching |
| type III: composite devices | | |
| device D | PVP with $MoS_2$ (10 wt%) | non-memory |
| device E | PVP with $MoS_2$ (20 wt%) | non-memory |
| device F | PVP with $MoS_2$ (30 wt%) | threshold switching |
| device G | PVP with $MoS_2$ (40 wt%) | bipolar switching |

trigonal prismatic structure [15]. The 2H phase has an energy gap of $\sim$ 1.9 eV [16], thus is suitable for switching memory devices, transistors, and solar cells [15]. The electronic properties of $MoS_2$ have been well studied. Ohmic behaviour in pressed pellet form [14], bipolar memory switching in bare $MoS_2$ system with Cu and $W_2N$ electrodes [17], and three different switching types, i.e., bipolar, asymmetric bipolar, and threshold switching (TS), in the same sample of $MoS_2$ and polyvinyl pyrrolidone (PVP) with Al and indium doped tin oxide (ITO) electrodes [18] have been reported. Wu et al. [19] have also shown that the energy consumption in the Pt/$MoS_2$ + PVP/ITO ReRAM can be significantly lowered by doping $MoS_2$ with nitrogen. That reveals the unpredictability of $MoS_2$ in different forms and different systems. In this work, we present a systematic study of resistive switching (RS) in devices with an active layer comprising: (1) bare PVP, (2) bare $MoS_2$, (3) PVP/$MoS_2$ bilayer, and (4) PVP + $MoS_2$ nanocomposite with different $MoS_2$ wt% (10–40 wt%). All devices were fabricated with Al and Ag, as BE and TE, respectively.

## 2. Experimental details

### 2.1. Solution preparation

The PVP (Sigma Aldrich, Prod. No. PVP40) and the $MoS_2$ (Sigma Aldrich, Prod. No. 234842) powders with a particle size $< 2\mu$m were separately dissolved in isopropyl alcohol (IPA) to produce 2.5 and 1 w/v% PVP and $MoS_2$ solutions, respectively. Both solutions were stirred for 4 h at room temperature.

### 2.2. Device Fabrication

Al sheet (Sigma Aldrich) was cut and pasted on a glass microscope slide and pre-cleaned by sonication (in acetone, then IPA, and lastly in ultra distilled water, each for 5 min). Active layers consisting of:

1. 1.4 $\mu$m thick $MoS_2$ (device A),
2. 1.01 $\mu$m thick PVP (device B),
3. 1.2 $\mu$m thick PVP on 1.36 $\mu$m thick $MoS_2$ bilayer (device C), and
4. 1.50 $\mu$m thick PVP + $MoS_2$ nanocomposites with 10 (device D), 20 (device E), 30 (device F) and 40 wt% (device G) $MoS_2$,

were spin-coated on the Al BE. Ag paste (Sigma Aldrich, Prod No. 735825) was applied on the top of the active layer as TE. Table I contains the notation used to describe all the fabricated devices.

### 2.3. Device characterization

Atomic force microscope (AFM, Nanosurf Flex-AFM) and field-effect scanning electron microscopy (FEG-SEM, JEOL JSM-7800F) equipped with an energy dispersive X-ray spectrometer (EDS, Oxford AZtec 350 X-Max80) were used to study morphology and estimate the thickness and the chemical composition of the active layers, respectively. In addition, electrical studies were conducted using precision source/measure unit (SMU, Keysight B2901A), connected as shown in Fig. 1.

## 3. Results and discussion

### 3.1. Topology and composition

Figure 2a and b is high-resolution FEG-SEM micrographs of devices C and G, respectively. To acquire an image, a highly energetic electron beam from the SEM's field emission gun was incident on the samples. Because of the high energy of this electron beam, the sample can be penetrated to some length, allowing the reconstruction of a 3D image of the sample from the back-scattered electrons. Our SEM results reveal that in both samples, $MoS_2$ appeared in the form of agglomerates of different sizes. In device C, where the $MoS_2$ bottom layer is under the PVP layer, SEM would only examine the PVP layer. However, our results reveal that large $MoS_2$ agglomerates from the bottom layer penetrated the PVP top layer and were detected by the SEM. In device G, however, our SEM results show an even

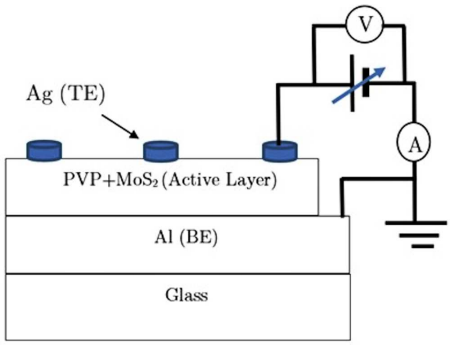


Fig. 1. A schematic diagram showing the cross-section of a typical ReRAM cell and the $I$–$V$ measurement scheme.

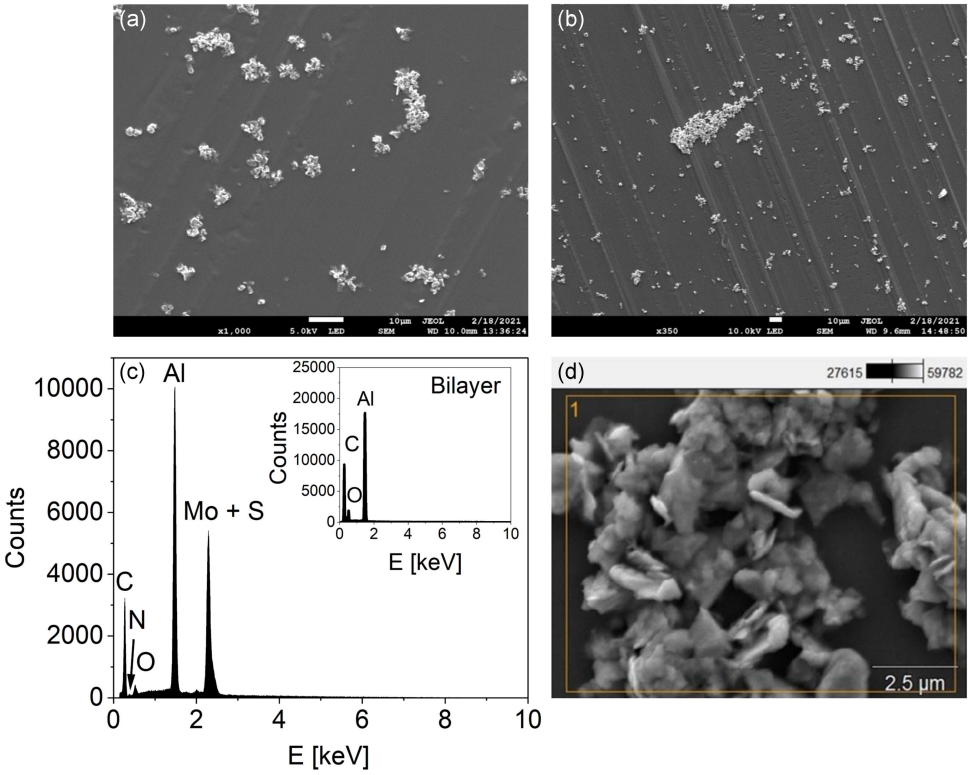


Fig. 2. Panels (a) and (b) are FEG-SEM micrographs of the active layer of device C and device G, respectively, while (c) is the EDS spectrum of device G (main graph) and device C (inset). Lastly, (d) is the magnified FEG-SEM micrograph of the $MoS_2$ agglomerate inside a PVP polymer.

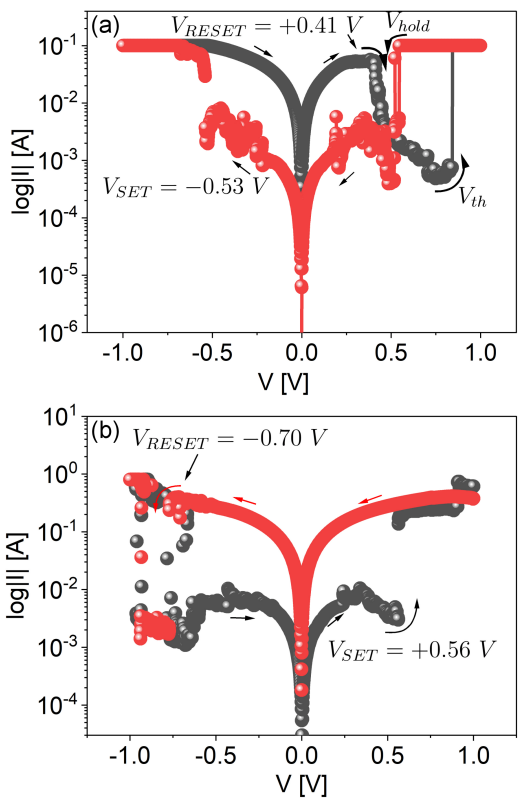


Fig. 3. The $I$–$V$ characteristics of (a) device C and (b) device G in semi-logarithmic scale.

dispensation of $MoS_2$ particles, such that even agglomerates having a small size are visible in the micrograph as expected. Figure 2c shows the EDS results taken from the surface of device G and device C (inset). As expected, $MoS_2$ traces were found only on the composite film. Lastly, Fig. 2d depicts the magnified SEM image of a cluster of $MoS_2$ particle, which reveals that the $MoS_2$ used in this study had flakes like 2D form.

### 3.2. Electrical studies

Current–voltage ($I$–$V$) data of device A with a single $MoS_2$ active layer and device B with a single PVP as the active layer did not show any resistive switching.

Figure 3 shows the semi-logarithmic $I$–$V$ characteristics of (a) device C and (b) device G. The $I$–$V$ characteristics of both devices reveal symmetric "S-type" bipolar memory behaviour [20, 21] with ON/OFF $\geq 10^2$ and very low operating voltages ($V_{\mathrm{SET}} = -0.50$ and $V_{\mathrm{RESET}} = +0.40$ V for device C, and $V_{\mathrm{SET}} = +0.56$ and $V_{\mathrm{RESET}} = -0.70$ V for device G).

Furthermore, in device C, a TS is observed (with $V_{\mathrm{hold}} = +0.54$, while $V_{\mathrm{th}} = +0.80$ V) beyond +0.40 V. This TS is not observed for negative voltage bias in this device. Even though a TS behaviour in ReRAMs is expected when a high compliance current ($I_{CC}$) is applied, the presence of this TS

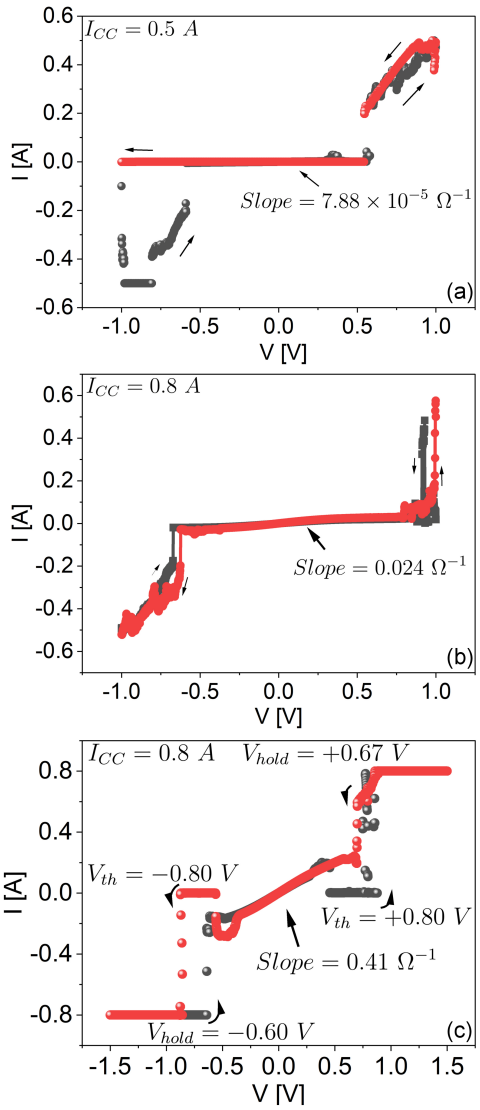


Fig. 4. The $I$–$V$ characteristics of (a) device D, (b) device E, and (c) device F.

in only one voltage polarity is an uncommon behaviour. In contrast, no TS was observed in device G, despite the large $I_{CC} = 0.8$ A used. Instead, somewhat multiple switching is observed only in the positive voltage polarity. The change in RS due to manipulation of active layers has been reported by Sun et al. [22]. Their results showed asymmetric TS in Al/$TiO_2$/Pt, symmetric bipolar RS in Al/DNA/Pt, asymmetric bipolar RS in Al/$TiO_2$–DNA/Pt bilayer, and multiple switching in Al/$TiO_2$–Graphene–DNA/Pt [22]. These results show that stalking different layers as an active layer significantly changes the electric transport and switching in the device. This difference in the RS behaviour of devices C and G may arise because of the unique nature of active layers used in the two devices.

Figure 4 shows the $I$–$V$ characteristic of (a) device D, (b) device E, and (c) device F. All the presented results show a linear variation in the current with the applied voltage before switching. Linear fits to these graphs yield slopes of $7.89 \times 10^{-5}$, $2.4 \times 10^{-2}$, and $4.1 \times 10^{-1}\ \Omega^{-1}$, respectively. This increase in slope may signify an increase in electrical conductivity with increasing $MoS_2$ content in the nanocomposite layer. RS in these devices occurs at low voltages of about ±0.60 V. Although devices D and E exhibit a jump from HRS to LRS, the current retraces its path by changing voltage sweep direction, showing no significant hysteresis. This behaviour signifies a non-memory-like character of the device. On the other hand, device F exhibits a TS for voltages greater than ±0.6 V with $V_{\mathrm{hold}}$ and $V_{\mathrm{th}}$ of ±0.60 and ±0.80 V, respectively.

Thus, it appears that the memory behaviour in PVP + $MoS_2$ nanocomposite devices can be controlled by controlling the amount of $MoS_2$. In the following subsection, we shall analyse devices C and G's conduction mechanisms, as these devices exhibited optimal memory behaviour.

### 3.3. Conduction mechanisms and RS in devices C and G

To understand the conduction mechanism leading to the RS in ReRAM devices, one can estimate the value of $n$ for the current density and voltage relationship, i.e., $J \propto V^n$ [23–25]. Figure 5a and b shows the $\ln(I)$ vs $\ln(V)$ relations corresponding to device C, while Fig. 6 — corresponding to device G. The $\ln(I)$–$\ln(V)$ graphs for both device C and G show that $n \simeq 1$, in the ON-state, indicative of Ohmic behaviour, i.e., $J \propto V$ [26]. This Ohmic behaviour in the ON-state current suggests the presence of conduction filaments (CFs). To understand the mechanism of the formation of these CFs in both systems, an analysis of the OFF-state current must be done. The OFF-state current variation of device C shows two distinct regions, namely, regions $i$ and $ii$, as shown in Fig. 5a. In region $i$, the current variation is very clear, without any noise, and is fitted very well with the linear fit ($n = 1$) with a very small (0.0023) standard error. In region $ii$, however, we see a large fluctuation, because of which we believe that the active layer is now preparing itself for the resistive switch. As such, any fit in this region is ambiguous. After trying different fits, the linear fit with $n \simeq 1.8$ was our best fit, with $R^2 = 0.698$ and standard error of 0.070. Figure 5b shows the magnification of the region $ii$. Though linear fit is weak, one can notice that despite the noise, the current seems to take a trajectory with a larger $n > 1$ value compared to region $i$. The value $n = 1.8$ obtained in this region weakly gives a trend pointing towards the possibility of the Mott–Gurney law ($J \propto V^2$) [26], i.e.,

$$J = \frac{9}{8} \frac{\varepsilon \varepsilon_0 \mu}{D^3} V^2. \tag{1}$$

where $\varepsilon$, $\varepsilon_0$, $\mu$ and $D$ are the permittivity, permittivity of free space, electronic drift mobility, and the active layer thickness, respectively.

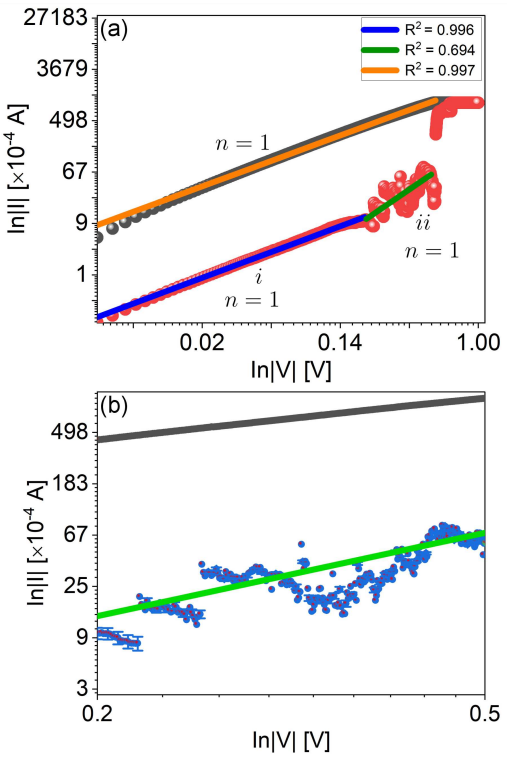


Fig. 5. The dependency $\ln(I)$ versus $\ln(V)$ of device C, showing the entire forward and reverse sweep of the negative voltage bias (a) and (b) the magnified graph of region *ii*.

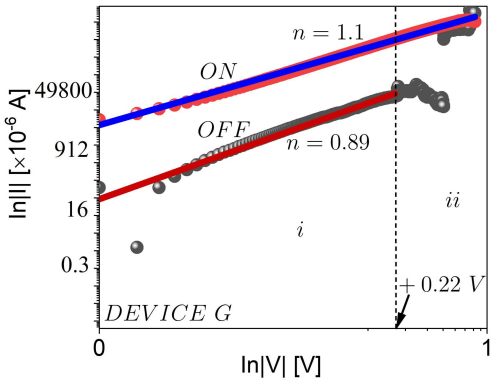


Fig. 6. The dependency $\ln(I)$ versus $\ln(V)$ of device G.

The occurrence of $J \propto V$ and $J \propto V^2$ in two consecutive regions implies that the possible mechanism taking place in device C is the space-charge limited conduction (SCLC) [5, 27], with transition voltage $V_{\rm tr} = 0.24$ V. The TS observed in a positive voltage bias is not understood. However, others have reported that the TS can be caused by a large $I_{CC}$ [28] or by other unidentified reasons [26, 27, 29, 30]. The large $I_{CC}$ used in our measurements provides room for TS to occur because of the Joule heating [31]. The conduction mechanism in device G differs from that in device C. The OFF-state current of device G follows a linear behaviour ($n = 0.89 \approx 1$) in the low voltage regime, i.e., region *i* (0–0.22 V). Beyond this voltage, i.e., in region *ii*, a decrease followed by an abrupt increase in the current occurs, taking the device to LRS. This behaviour deviates from the SCLC behaviour displayed by device C. We shall attempt to explain it.

When a potential is applied, say at the Ag electrode, there is electron accumulation at the Al electrode, while the Ag has electron deficiency. These electrons can tunnel through the Al/PVP + $MoS_2$ interface into the active layer containing the $MoS_2$ particles, resulting in the trend seen in region *i* [32]. According to Shinde et al. [33], this charge can be trapped because of the low energy level or quantum confinement effect in the $MoS_2$ system, which can explain the trend observed in region *ii*. When the voltage is sufficiently high, electrons gain enough energy and jump to the conduction band of the $MoS_2$ in the nanocomposite [34], resulting in high conductivity and hence HRS-to-LRS switching. Conduction behaviour observed in our devices differs from that reported for the Al/$MoS_2$ & PVP/ITO [18], ITO/N-doped $MoS_2$–PVP/Pt [19], and Ag/ $MoS_2$–PVP/Ag [34] devices. This comparison shows that the type of electrodes, nanocomposite constitution and composition play essential roles in conduction mechanisms in these polymeric ReRAMs.

## 4. Conclusion

Resistive switching at voltages as low as 0.56 V has been achieved in $MoS_2$ embedded PVP nanocomposite films of micrometre thickness, and much lower ($<$ 0.56 V) switching voltages could be achieved in micrometre-thick PVP/$MoS_2$ bilayers. Ultra low voltage resistive switching is essential for low power consumption ReRAMs and futuristic energy-efficient computers. We showed different conduction and resistive switching behaviour for ReRAM devices characterized by different active layers, namely *i* $MoS_2$ embedded PVP nanocomposite films and *ii* a bilayer system of $MoS_2$ and PVP micron layers. These studies reveal the variety of resistive switching and conduction mechanisms achievable by manipulating the active layer consisting of PVP and $MoS_2$ for the same set of electrodes. We can conclude that memory behaviour can be induced and manipulated by controlling the nature of the active layer and the amount of $MoS_2$ dispersed in the PVP nanocomposite.

## Acknowledgments

ZWD acknowledges the New Generation of Academics Program (nGAP) support provided by DHET through CUT and the DST/NRF for the S&F-Research Development Grant for nGAP Scholars.

## References


[1] G. Li, Y. Hou, A. Wu, *Chin. Geogr. Sci.* **27**, 626 (2017).

[2] G.P. Fettweis, E. Zimmermann, in: *11th Int. Symp. on Wireless Personal Multimedia Communications (WPMC 2008)*, 2008 p. 2006.

[3] T.W. Hickmott, *J. Appl. Phys.*, **33**, 2669 (1962).

[4] D.S. Jeong, R. Thomas, R.S. Katiyar, J.F. Scott, H. Kohlstedt, A. Petraru, C.S. Hwang, *Rep. Prog. Phys.* **75**, 076502 (2012).

[5] S. Vallabhapurapu, S. Dub, A. Srinivasan, *Electronics: Nonvolatile Memory Technologies*, in: *Encyclopedia of Polymer Applications*, 1st Ed., 2018, p. 913.

[6] S. Liu, S. Dong, X. Wang, L. Shi, H. Xu, S. Haung, J. Luo, *Nanotechnology* **31**, 255204 (2020).

[7] S. Vallabhapurapu, L.D.V. Sangani, M.G. Krishna, V.V. Srinivasu, C. Du, S. Du, A. Srinivasan, *Mater. Today Proc.* **9**, 615 (2019).

[8] T.L. Tsai, H.Y. Chang, J.J.C. Lou, T.Y. Tseng, *Appl. Phys. Lett.* **108**, 153505 (2016).

[9] A.T. Fabiyi, S. Vallabhapurapu, I.O. Osunmakinde, in: *2019 Open Innovations (OI)*, IEEE, Cape Town 2019, p. 211.

[10] C. Zhong, W. Tzeng, K. Liu et al., *Surf. Coat. Technol.* **231**, 563 (2013).

[11] N. Raeis Hosseini, J.-S. Lee, *ACS Nano* **9**, 419 (2015).

[12] S. Vallabhapurapu, L. D. V. Sangani, M.G. Krishna, J. Das, A. Srinivasan, V.V. Srinivasu, *J. Mater. Sci. Mater. Electron.* **32**, 3556 (2021).

[13] H. Wang, B. Zhu, H. Wang, X. Ma, Y. Hao, X. Chen, *Small* **12**, 3360 (2016).

[14] O. El Beqqali, I. Zorkani, F. Rogemond, H. Chermette, R.B. Chaabane, M. Gamoudi, G. Guillaud, *Synth. Met.* **90**, 165 (1997).

[15] X. Li, H. Zhu, *J. Mater.* **1**, 33 (2015).

[16] M. Acerce, D. Voiry, M. Chhowalla, *Nat. Nanotechnol.* **10**, 313 (2015).

[17] R. Prakash, S. Sharma, A. Kumar, D. Kaur, *Curr. Appl. Phys.* **19**, 260 (2019).

[18] N. Bai, M. Xu, C. Hu, Y. Ma, Q. Wang, D. He, J. Qi, Y. Li, *Mater. Sci. Semicond. Process.* **91**, 246 (2019).

[19] Z. Wu, T. Wang, C. Sun, P. Liu, B. Xia, J. Zhang, Y. Liu, D. Gao, *AIP Adv.* **7**, 125213 (2017).

[20] D. Prime, S. Paul, *Philos. Trans. R. Soc. A Math. Phys. Eng. Sci.* **367**, 4141 (2009).

[21] S. Vallabhapurapu, L.D.V. Sangani, M.G. Krishna, J. Das, C. Tu, S. Du, A. Srinivasan, *Acta Phys. Pol. A* **134**, 68 (2018).

[22] B. Sun, S. Ranjan, G. Zhou, T. Guo, Y. Xia, L. Wei, Y.N. Zhou, Y.A. Wu, *Mater. Today Adv.* **9**, (2021).

[23] Y. Liu, P. Gao, X. Jiang, L. Li, J. Zhang, W. Peng, *J. Appl. Phys.* **116**, 064505 (2014).

[24] S. Vallabhapurapu, A. Rohom, N.B. Chaure, C. Tu, S. Du, V.V. Srinivasu, A. Srinivasan, *Appl. Phys. A* **124**, 639 (2018).

[25] Z.W. Dlamini, S. Vallabhapurapu, O.A. Daramola, P.F. Tseki, R.W.M. Krause, S. Xavier, T.S. Mahule, S.V. Vallabhapurapu, *J. Circuits Syst. Comput.* **31**, 2250113 (2022).

[26] F. Chiu, *Adv. Mater. Sci. Eng.* **2014**, 1 (2014).

[27] K.T. Patil, K.A. Nirmal, S.A. Jadhav, S.R. Patil, T.D. Dongale, D. Kim, P.S. Patil, *Materialia* **15**, 101026 (2021).

[28] U. Das, A. Nyayban, B. Paul, A. Barman, P. Sarkar, A. Roy, *ACS Appl. Electron. Mater.* **2**, 1343 (2020).

[29] C. Pan, Y. Ji, N. Xiao et al., *Adv. Funct. Mater.* **27**, 1604811 (2017).

[30] Y.J. Huang, S.C. Chao, D.H. Lien, C.Y. Wen, J.H. He, S.C. Lee, *Sci. Rep.* **6**, 1 (2016).

[31] Y.C. Yang, F. Pan, F. Zeng, *New J. Phys.* **12**, 023008 (2010).

[32] B. Singh, B.R. Mehta, *Thin Solid Films* **569**, 35 (2014).

[33] S.M. Shinde, G. Kalita, M. Tanemura, *J. Appl. Phys.* **116**, 214306 (2014).

[34] M.M. Rehman, G.U. Siddiqui, J.Z. Gul, S.W. Kim, J.H. Lim, K.H. Choi, *Sci. Rep.* **6**, 1 (2016).